

Article

Spatiotemporal Analysis of Sonar Detection Range in Luzon Strait

Gengming Zhang ¹, Lihua Zhang ^{1,*}, Yitao Wang ^{2,*}, Yaowei Ma ¹, Xingyu Zhou ¹ and Yue Yu ³¹ Department of Military Oceanography and Hydrography, Dalian Naval Academy, Dalian 116000, China; zhanggengming1999@163.com (G.Z.); shhcube@163.com (Y.M.); 13805488150@163.com (X.Z.)² Software and Simulation Institute, Dalian Naval Academy, Dalian 116000, China³ Unit 92538, Dalian 116000, China; 18640819235@163.com

* Correspondence: zlhua@163.com (L.Z.); wytbmdx@163.com (Y.W.)

Abstract: Sonar serves as a critical submarine detection apparatus for naval vessels, with its detection range forming the foundation of its overall performance in underwater surveillance. The Luzon Strait, in the eastern part of the South China Sea, presents a complex hydrographic setting that profoundly influences sonar performance, necessitating mastery of the detection range variation for enhanced anti-submarine operational efficiency. This study employs the Bellhop acoustic propagation model to estimate the transmission loss. Subsequently, a detection probability integration approach is applied to determine the sonar detection range in the Luzon Strait from 2019 to 2023, which is then subjected to statistical analysis. The findings indicate the following. (1) During the summer and autumn, the shallow mixed layer fails to generate a surface duct, resulting in shorter detection ranges that are primarily dependent on the water depth. In the Shallow Water Zone (<150 m), frequent interactions between sound waves and the sea boundaries lead to considerable acoustic energy attenuation, maintaining a short detection range. In the Intermediate Depth Zone (150–2500 m), sound rays retain adequate energy post-seabed reflection, extending the sonar detection to 5–8 km. Beyond 2500 m, the diminishing reflective energy restricts the range to 2–5 km. (2) Conversely, in the winter and spring, the formation of a surface duct becomes the predominant determinant of the detection range, capable of exceeding 10 km, overshadowing the influence of the water depth.

Keywords: Luzon Strait; sonar detection range; Bellhop acoustic propagation model; mixed layer depth



Citation: Zhang, G.; Zhang, L.; Wang, Y.; Ma, Y.; Zhou, X.; Yu, Y.

Spatiotemporal Analysis of Sonar Detection Range in Luzon Strait. *J. Mar. Sci. Eng.* **2024**, *12*, 1191. <https://doi.org/10.3390/jmse12071191>

Academic Editor: Sergei Chernyi

Received: 7 June 2024

Revised: 21 June 2024

Accepted: 25 June 2024

Published: 16 July 2024



Copyright: © 2024 by the authors. Licensee MDPI, Basel, Switzerland. This article is an open access article distributed under the terms and conditions of the Creative Commons Attribution (CC BY) license (<https://creativecommons.org/licenses/by/4.0/>).

1. Introduction

In modern warfare, the continuous integration of advanced technologies into submarines has led to a progressive enhancement of their combat capabilities and survivability. The speed of new nuclear submarines now rivals that of surface vessels, making it considerably easier for them to occupy attack positions. Confronted with the escalating underwater threat, submarine detection has become a paramount task for surface fleet formations [1]. Passive sonar systems are crucial to the submarine alert capabilities [2]. The search for underwater targets is typically characterized as a process where sonar systems maximize coverage of the relevant area. The sonar detection range (DR) commonly refers to the ability of a sonar system to detect targets under specific target characteristics and environmental constraints. It is considered the foundation for the performance of tracking and identification capabilities [3]. When naval formations are conducting submarine search or alert missions, parameters such as the spacing between vessels should be established in reference to the sonar DR [4]. Additionally, the deployment of unmanned platforms, such as unmanned undersea vehicles (UUVs), for underwater detection and penetration missions [5–7], as well as collaborative detection and tracking by multiple platforms, rely on the sonar detection range for mission planning [8]. Consequently, mastering the spatiotemporal variation patterns of the DR is critical for the configuration of surface vessel

anti-submarine positions and for the planning of mission paths for various sonar platforms engaged in maritime anti-submarine detection.

Straits, as relatively narrow waterways connecting two seas or oceans between two landmasses, serve as vital maritime transportation routes and shipping hubs, and they have historically been strategic points of contention for military forces [9–11]. The Luzon Strait, for instance, is a critical strait passage in the eastern part of the South China Sea, attracting extensive attention from various military powers. The complex topography of its seabed and the variable hydrographic environment in this area [12,13] cause refraction, scattering, and absorption of acoustic signals, all of which impact sonar performance [14,15]. In recent years, scholars in related fields have conducted extensive research on sonar detection capabilities. Liang et al. [16] simulated the propagation of sound waves in shallow water areas under three typical sound speed profiles, focusing on geometric transmission loss and medium absorption loss, and provided strategies for sonar usage under different hydrographic conditions. This research assumed a simplified layered structure for the sound speed profile without analyzing the actual profiles in the ocean. Emerson et al. [17] used detection probability curves to compare the sonar performance in two sea areas in the southern East China Sea. Detection probability curves can reflect the change in sonar performance with distance in a detailed manner, but they struggle to capture the spatiotemporal variability of sonar performance when the study area is large and there are numerous data points. Guo, Ai, Chen and Qi [3] investigated the impact of different detection probabilities on the DR based on the sonar equation. The method of manually determining the DR in the face of fluctuating transmission loss curves is poorly reproducible and not suitable for batch operations with a large number of research samples. Na et al. [18] built upon the DR by incorporating the robustness of detection (ROD), the ratio of the maximum DR to the width of the blind zone, to fully describe the spatiotemporal variation of sonar performance in the eastern sea area of Korea. However, using two parameters to describe sonar performance is not as intuitive. Previous studies have employed various metrics to investigate sonar performance; however, in the Luzon Strait, where the marine environment undergoes drastic changes, research into the spatiotemporal variability of the sonar detection range remains inadequate. This paper employs the methodology established by Ferla and Porter [19] to determine the optimal receiving depth for the calculation of the sonar detection range. This method initiates with the sonar equation and calculates the signal excess (SE) by utilizing the figure of merit (FOM) in conjunction with the transmission loss (TL). The TL is obtained through the use of an acoustic propagation model, which requires the input of the underwater acoustic environment to calculate. Subsequently, the detection probability is derived using probabilistic methods, and the integration of this probability yields the detection range (DR). Due to phenomena such as acoustic wave interference, the TL curves exhibit high-frequency oscillations. By integrating them to determine the DR, this method avoids errors caused by manual selection due to oscillations, facilitating long-term statistical analysis of the DR in the Luzon Strait area.

In the Section 2, Data and Methods section of this paper, a description is provided of the temperature and salinity data, as well as the water depth data, employed in the study. Furthermore, a detailed introduction is provided to the integral calculation method for sonar DR. In the Section 3, Results section, a comprehensive analysis of the temporal and spatial variations of the DR in the Luzon Strait is conducted, aiming to uncover its intrinsic patterns. In the Section 4, Discussion section, the impact of the water depth and mixed layer depth on the regional DR in the Luzon Strait area is explored, and the necessity and feasibility of predicting the DR under limited data conditions are discussed. In the Section 5, Conclusion section, a summary of the spatiotemporal patterns of the DR changes in the Luzon Strait is presented, and potential future research directions are proposed.

2. Data and Methods

2.1. Data

The present study utilizes sound velocity derived from the Mackenzie empirical formula, using the ocean temperature and salinity data obtained from the Hybrid Coordinate Ocean Model (HYCOM), to conduct an analysis of the sound propagation characteristics in the Luzon Strait. Developed through a collaboration between the University of Miami, the Naval Research Laboratory (NRL), and the Los Alamos National Laboratory (LANL), HYCOM is capable of assimilating prior oceanographic observations at high resolutions (with horizontal resolution of $1/12^\circ$), providing a three-dimensional reanalysis of oceanographic data [20–22]. For the purpose of this study, a total of 168 experimental sites were selected within the region bounded by $16\text{--}25^\circ$ N latitude and $115\text{--}125^\circ$ E longitude, at a spatial resolution of 0.5° for both latitude and longitude (the locations of these sites are depicted in Figure 1). The data utilized for the analysis spanned a period of five years (from January 2019 to December 2023), with a temporal resolution of 10 days.

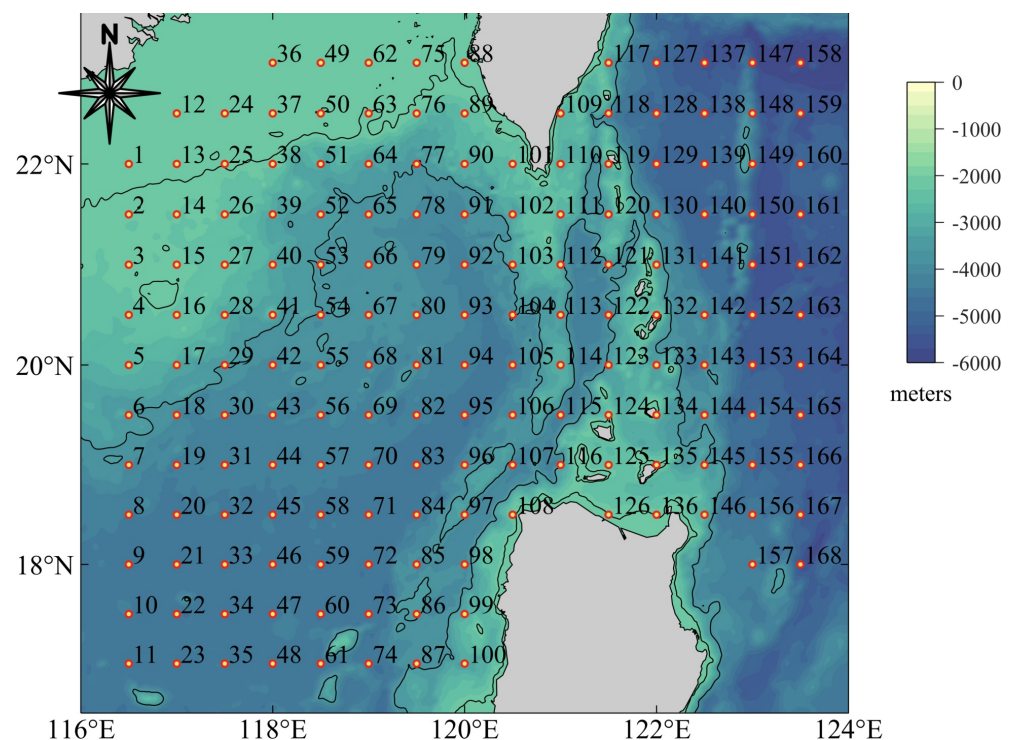


Figure 1. Distribution map of experimental points in the research sea area. (The different numbers in the figure represent the codes for the experimental sites).

The bathymetric data for this study are derived from ETOPO 2022, a global bathymetry and topography dataset with enhanced resolution of 15 arc-seconds. This dataset provides a comprehensive, high-resolution depiction of the Earth's surface physical features by integrating topographic, bathymetric, and coastline data from both regional and global sources. It incorporates the latest advancements in data sources and processing techniques since the release of ETOPO1 in 2010. The ETOPO 2022 model utilizes a combination of various airborne light detection and ranging (LiDAR), satellite altimetry, and shipborne bathymetry datasets from the United States, significantly improving the relative and absolute horizontal and vertical geolocation accuracy of the global topographic model. This dataset is employed as an input for the bathymetric field in the underwater acoustic propagation model.

2.2. Research Methods

2.2.1. Modeling Sound Propagation Loss Using Bellhop

The sonar equation serves as the logical foundation for calculating the DR through the use of acoustic parameters [23,24]. The form of the passive sonar equation is:

$$SE = (SL - TL) - (NL - DI) - DT \quad (1)$$

where SE is the signal excess, SL is the source level, TL is the transmission loss, NL is the ambient noise level of the marine environment, DI is the directivity index of the receiving array, and DT stands for the detection threshold. TL is a function of the propagation distance and depth, influenced by the distribution of the ocean's sound speed field, and it is crucial for predicting sonar performance. The Bellhop acoustic model is employed to calculate the transmission loss, utilizing a Gaussian beam-tracing method that leverages a given sound speed field for ray tracing and the computation of the transmission loss. The Bellhop model, when calculating acoustic fields within a frequency range of 0.6 to 30 kHz, demonstrates excellent agreement with experimental data and has been designated as the standard model for predicting ocean acoustic propagation within the frequency band of 10 to 100 kHz by the United States Navy [25,26].

The beam pattern centered around the source axis is represented by the following expression for the acoustic pressure field:

$$P(s, n) = A(s)\phi(s, n)e^{-i\omega\tau(s)} \quad (2)$$

where s represents the arclength along the central ray; n denotes the normal distance from the neighboring receiving position to the central ray; ω is the angular frequency of the signal; and $\tau(s)$ signifies the signal delay.

For a beam with a Gaussian profile, the parameters $A(s)$ and $\phi(s, n)$ can be expressed as follows:

$$A(s) = A_0 \sqrt{\frac{c(s)}{q(s)}} \quad (3)$$

$$\phi(s, n) = e^{-i\omega(p(s)/2q(s))n^2} \quad (4)$$

where A_0 represents a constant that is related to the type of sound source; and $p(s)$ and $q(s)$ are the beam width and curvature, respectively, and are governed by the following pair of differential equations:

$$\frac{dq}{ds} = c(s)p(s) \quad (5)$$

$$\frac{dp}{ds} = \frac{c_{nn}}{c^2(s)}q(s) \quad (6)$$

where c_{nn} denotes the second derivative of the sound speed in the direction normal to the acoustic ray path.

Upon computation of the acoustic intensity, the transmission loss is subsequently derived in accordance with the established definition:

$$TL = -20 \lg \left| \frac{P}{P_{rf}} \right| \quad (7)$$

where P_{rf} represents the acoustic pressure at a distance of 1 m from the center of the sound source.

The Bellhop model is capable of effectively simulating sound sources within the frequency range of 0.6–30 kHz [27]. Calculations of the transmission loss are performed at each point in eight directions by Bellhop (true azimuths of 0°, 45°, 90°, 135°, 180°, 225°, 270°, and 315°). For these computations, the sound source frequency is set to 1000 Hz, and both the source depth (SD) and the receiver depth (RD) are established at 50 m.

2.2.2. Methodology for Estimating Detection Range

This study concentrates on the intricate marine conditions prevalent in the Luzon Strait, examining their influence on the acoustic transmission loss as a means of evaluating the performance of passive sonar systems. The *FOM* is utilized to denote the minimal permissible one-way transmission loss for the successful reception of acoustic signals by passive sonar, and it is computed according to the following formula:

$$FOM = SL - NL + DI - DT \quad (8)$$

The sound signal margin (*SE*) received by the sonar is:

$$SE = FOM - TL \quad (9)$$

Conventional approaches to quantifying the detection range (*DR*) rely on the equation $SE(DR) = 0$, yet the variability of the transmission loss (*TL*) over distance frequently yields multiple *DR* values that fulfill $SE(DR) = 0$, complicating the precise determination of the propagation distance. In the research conducted by Guo, Ai, Chen and Qi [3], the intersection points of the *FOM* and *TL* curves were manually identified to ascertain the *DR* values, given the limited dataset, which provided a convenient and swift technique. However, given the extensive *TL* data involved in the current study, a manual approach is impractical for processing large datasets and introduces a higher degree of subjectivity. Hence, this paper incorporates the methodology of Ferla and Porter [19], originally devised for determining the optimal receiving depth, to calculate the *DR*. The procedure is initiated by introducing the detection probability function:

$$P_D(SE) = \frac{1}{\sqrt{2\pi}\sigma} \int_{-\infty}^{SE} \exp\left(\frac{-x^2}{2\sigma^2}\right) dx \quad (10)$$

When the signal excess (*SE*) is zero, the detection probability reaches a median level of 50%. The parameter σ serves to regulate the steepness of the curve, and it is set to 8 in here [19]. Following this, the integration of P_D across the range (*r*) in a fixed sound source depth (*z*) yields an estimation of the detection range:

$$DR = \int_0^{\infty} P_D(SE, r, z) dr (P_D > 0.5) \quad (11)$$

2.2.3. The Advantages of Integration Methodology

Figure 2 presents a *TL* curve diagram, where the horizontal line indicating $TL = 85$ dB represents the *FOM*. The determination of the *DR* necessitates an analysis of the nexus between the *TL* and the *FOM*. It can be observed from the figure that the *TL* and *FOM* curves intersect frequently, which complicates the issue if $SE(DR) = 0$ is used for the assessment. However, by employing Equation (11) described above, a single, definitive *DR* value of 33.2 km can be calculated. Indeed, as the distance exceeds 30 km, the *TL* curve exhibits a marked convergence with the *FOM* value, indicative of a reduced *SE*. Consequently, it can be deduced that the effective *DR* is approximately 30 km. This demonstrates that the integral method not only maintains computational rigor but also yields results that closely align with human perception. In such cases, this method can automatically process a large amount of *TL* data to produce reliable outcomes.

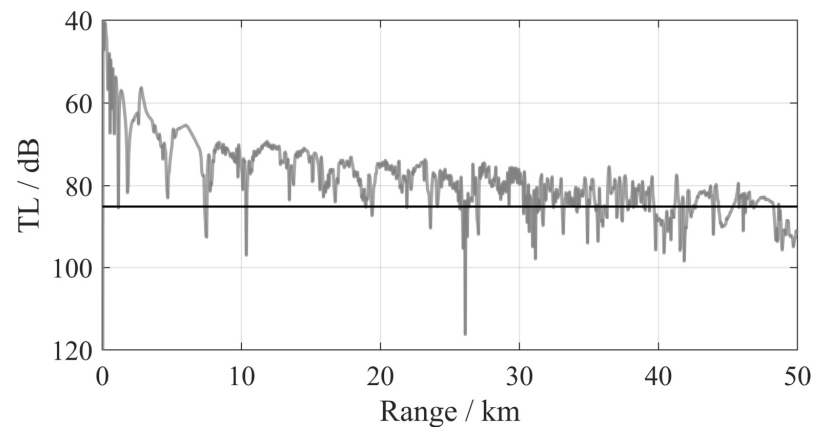


Figure 2. Nexus between *TL* and *FOM* (*FOM* = 85 dB, black horizontal line).

3. Results

3.1. Overall Analysis of Spatiotemporal Changes in Detection Range

The monthly statistical data from 2019 (Figure 3) reveal pronounced seasonal and spatial distribution patterns in the DR. Overall, the DR exhibits larger values during the spring and winter seasons, with distinct high-value areas, whereas it is smaller during the summer and autumn. In terms of the spatial distribution, the study area can be divided into three parts:

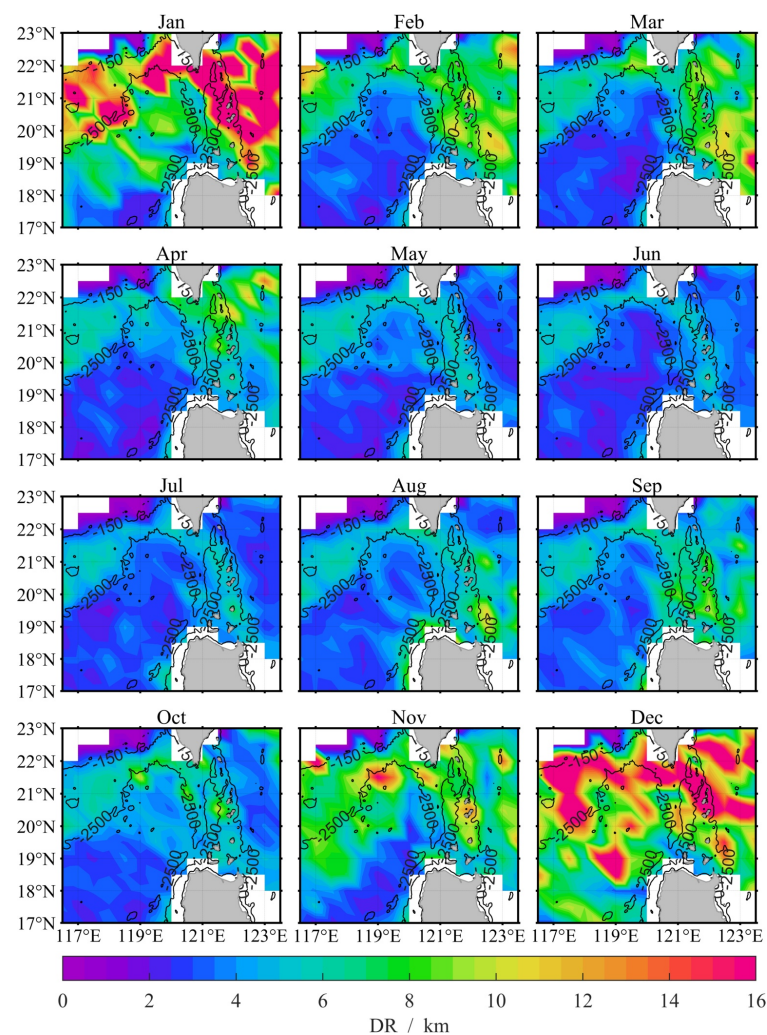


Figure 3. Monthly statistical data of sonar detection distance in 2019.

1. The Shallow Water Zone, which includes the continental shelf off the coast of Guangdong, China, within the 150 m isobath. In this region, the DR remains almost constant throughout the year and maintains the lowest values (1–2 km).
2. The Intermediate Depth Zone, ranging from 150 m to 2500 m isobaths, encompassing the broad lateral intermediate water zone in the northwestern part of the study area, as well as the regions around the Heng-Chun and Luzon Ridges in the Luzon Strait. In January, the Intermediate Depth Zone is mostly covered by high values, while from February to October, the DR largely stabilizes within 5–8 km, and from October to December, it is again gradually covered by high-value areas, with the maximum DR reaching up to 16 km.
3. The Deepwater Zone, including the basin region deeper than 2500 m located in the southwestern part and the deepwater area in the eastern part of the study area. Starting from January, the low-value areas of the DR (2–5 km) gradually expand northward, almost completely occupying the region within the 2500 m isobath by March. Thereafter, the DR in the southern part of the basin further decreases, with the low-value area reaching its maximum extent around May. From June, the low-value area in the basin begins to retract, almost disappearing by December. In the deepwater area east of Luzon Strait, the DR gradually decreases from January to July, then increases from August to December, exhibiting the largest range of variation throughout the year (3–16 km).

It is evident that the statistical results from 2019 to 2023 all exhibit the aforementioned distribution patterns of the DR and seasonal variations (which are not displayed here). To describe the interannual variations, the empirical orthogonal function (EOF) technique is employed. The EOF decomposes spatiotemporal data (X) into spatial modes (EOF) and temporal modes (PC):

$$X = EOF \times PC \quad (12)$$

The first mode (EOF-1) accounts for 67% of the variance. Its time series (PC-1) reaches a maximum in December and a minimum in June, capturing a strong seasonal cycle (Figure 4).

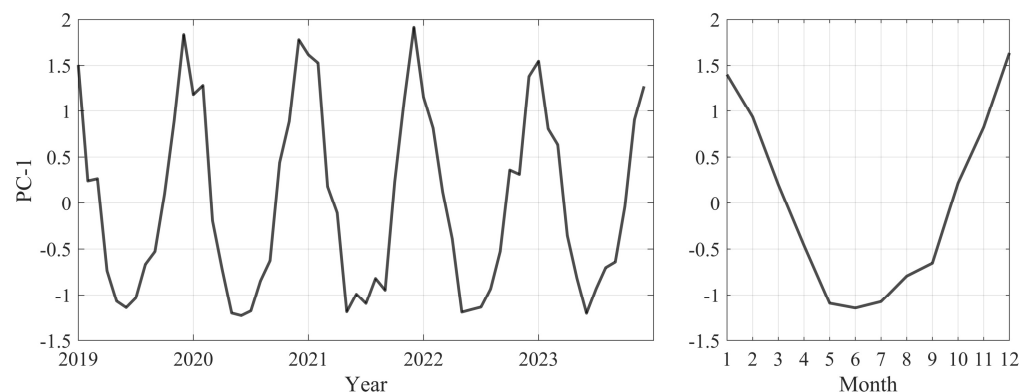


Figure 4. The amplitude time series (left) and average of each month (right) for the first EOF modes of the DR.

3.2. Sound Propagation Environment Analysis

3.2.1. Shallow Water Zone

The acoustic propagation environment in the Shallow Water Zone is intricate, with the seabed boundary exerting a significant influence on shallow water acoustic propagation. Within the limited depth of the sea, the distance of sound propagation is constrained, and the frequent reflection and absorption of sound waves by the seabed result in significant attenuation of acoustic energy [28]. Na, Cho, Son and Hahn [18] have also described this phenomenon. Consequently, the Shallow Water Zone adjacent to the coast of Guangdong, China, experiences a persistently low DR. This region is located at the periphery of the

study area and exhibits minimal temporal variation. Therefore, a specific analysis of its acoustic propagation environment is not conducted.

3.2.2. Intermediate Depth Zone

An experimental site (Point 27) located at approximately the center of the Intermediate Depth Zone, with coordinates (21° N, 117.5° E), is selected for the analysis of the acoustic propagation environment in the Intermediate Depth Zone. Figure 5a depicts the propagation loss of acoustic waves emitted from a source at a depth of 50 m, under the temperature and salinity conditions from January to December 2019, in an easterly direction. It is evident that the sound rays reflect off the seabed and propagate forward, manifesting as bright streaks. Each reflection with the seabed results in a loss of energy, causing the propagation loss streaks to gradually dim. For instance, within the range of 0–10 km from the sound source at a receiving depth of 50 m in June, the acoustic propagation loss initially increases, then decreases, and subsequently increases gradually, resulting in a peak in the curve within the range of 5–8 km (indicated by the red arrow in Figure 5b). This is due to the relatively small propagation loss after the first reflection of the sound wave, which still allows the *TL* to be below 85 dB (*FOM*) at the receiving depth of 50 m. As the number of reflections increases, the acoustic energy attenuates at the receiving depth and surpasses the *FOM*, resulting in a negative *SE*, thereby limiting the expansion of the DR.

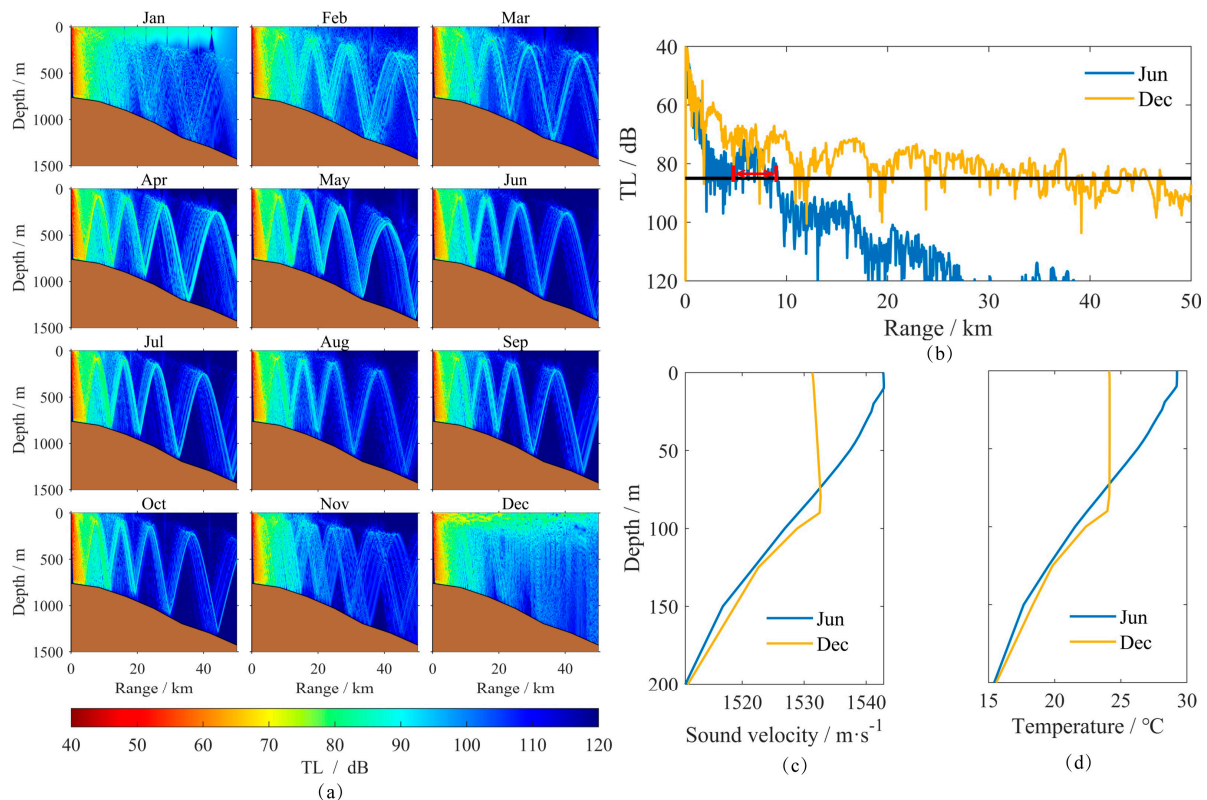


Figure 5. Analysis of sound propagation in the Intermediate Depth Zone (Point 27). (a) Two dimensional sound propagation loss; (b) Sound propagation loss curve; (c) Sound velocity profile; (d) Temperature profile.

In Figure 5a, the acoustic propagation loss map for December highlights a conspicuous zone of high acoustic energy within the water depth range of 0–100 m. This phenomenon is called a surface sound channel, ascribed to the positioning of the sound source within the mixed layer (Figure 5d indicates that the mixed layer is notably more profound during December in comparison to June), where the gradient of the sound speed is positive (Figure 5c). Sound propagation within the surface sound channel is constrained in depth,

with minimal diffusion. Consequently, the acoustic energy attenuates to a lesser extent at a receiving depth of 50 m, which is a contributing factor to the relatively extended DR observed in this region during January and December.

In the mixed layer, the temperature of seawater remains nearly constant with increasing depth while the sound speed is primarily influenced by pressure. Consequently, the sound speed in this layer exhibits a positive gradient, increasing with depth. Lorbacher et al. [29] utilized a curvature index based on the surface temperature to estimate the mixed layer depth (MLD), yielding satisfactory results. This study adopts the same methodology to statistically determine the MLD for the months of January, April, July, and October in 2019 within the study area. These values are designated to represent the depth distribution of the mixed layer for the winter, spring, summer, and autumn seasons, respectively, for the years 2019–2023 (Figure 6).

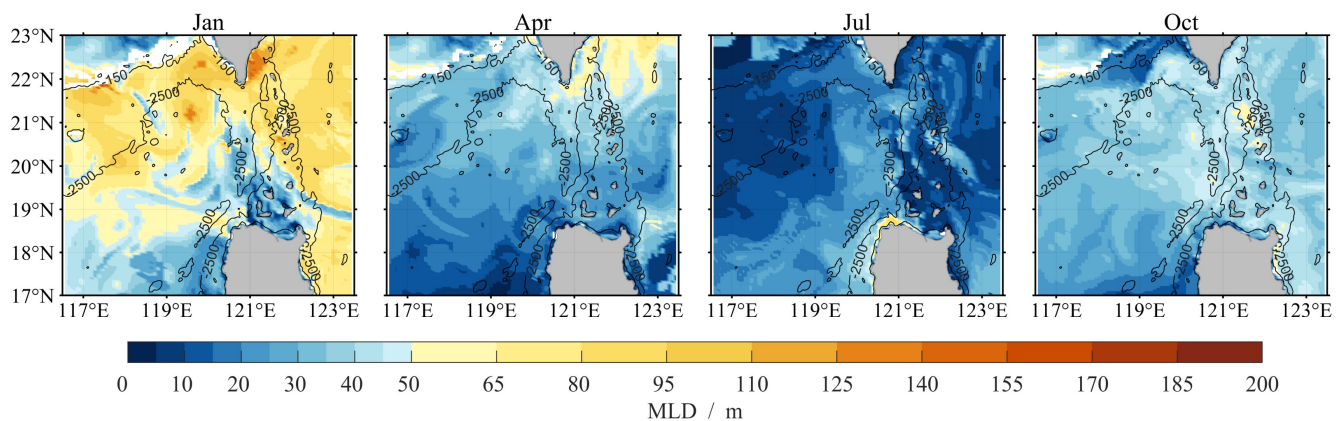


Figure 6. Distribution of mixed layer depth in the study area for the months of January, April, July, and October.

Multiple studies have indicated that the variability of the mixed layer depth (MLD) in the South China Sea is influenced by the wind, heat fluxes, freshwater fluxes, and solar shortwave penetration. Duan et al. [30] employed quantitative analysis to demonstrate a strong correlation between the intensity of the MLD in the South China Sea and the buoyancy flux. A negative buoyancy flux, which is primarily determined by the heat fluxes, signifies the instability of the surface water, leading to its downward motion and consequently a stronger MLD. From October to December, heat loss results in a mostly negative buoyancy flux in the northern South China Sea, and the buoyancy flux in central South China Sea experiences a transition from positive to negative. From January to April, there is a progressive enhancement of the buoyancy flux in the northern South China Sea. Despite this intensification, the buoyancy flux maintains negative values during January. The process described above contributes to a deep MLD in the northern region of the research area during winter and spring. The seasonal variability of the MLD calculated in this study is consistent with previous research findings. In January, the MLDs in the Intermediate Depth Zone and the deep-sea area east of the Luzon Strait all exceeded 50 m. This reflects the situation where the sound source is entirely within the mixed layer during the winter season. The emitted sound waves propagate as a surface sound channel, which is advantageous for long-distance detection. This explains the larger DR observed in January, February, March, November, and December of 2019 in the DR distribution map (with high value regions of 9–16 km). In April, July, and October, however, the areas with a mixed layer thickness exceeding 50 m significantly decreases. At this time, the majority of sound waves emitted from source would refract downward in a negative sound speed gradient environment, resulting in a significant reduction in the DR.

3.2.3. Deepwater Zone

The South China Sea Basin exhibits an overall low DR from February to September. With the onset of winter, the DR in the northern part of the basin gradually increases, separating from the low-value region in the southern part of the basin. The acoustic propagation environment in this region is analyzed at the experimental site Point 70, with coordinates 19° N, 119° E (Figure 7). This experimental site has an average water depth of approximately 4000 m, which is significantly deeper than Point 27, with a water depth of 800–1500 m. Sound waves emitted from the surface source refract toward the seabed in a negative sound speed gradient environment, undergoing a considerable horizontal displacement of approximately 20 km before reaching the seabed. In contrast, the horizontal displacement of sound waves at the first contact with the seabed at Point 27 is generally less than 5 km. Consequently, at Point 70, the sound waves typically undergo only 1–2 reflections off the seabed within a range of 50 km, with the maximum emerge reflection reaching the receiving depth at a horizontal displacement of up to 35 km, as indicated by the red arrow in Figure 7b. This peak, characterized by a substantial displacement and having undergone a longer propagation distance, has less energy than the reflection peak at Point 27. This results in the DR in the Deepwater Zone being approximately half that of the Intermediate Depth Zone when a surface sound channel is not present. When a surface sound channel is present, the DRs in both sea areas are similar and are almost unaffected by topographic factors. The deep-sea area east of the Luzon Strait, with its deeper water depth, does not produce reflection waves with sufficient energy to meet the detection requirements at the receiving depth, indicating that the DR is significantly influenced by the upper sound speed profile too.

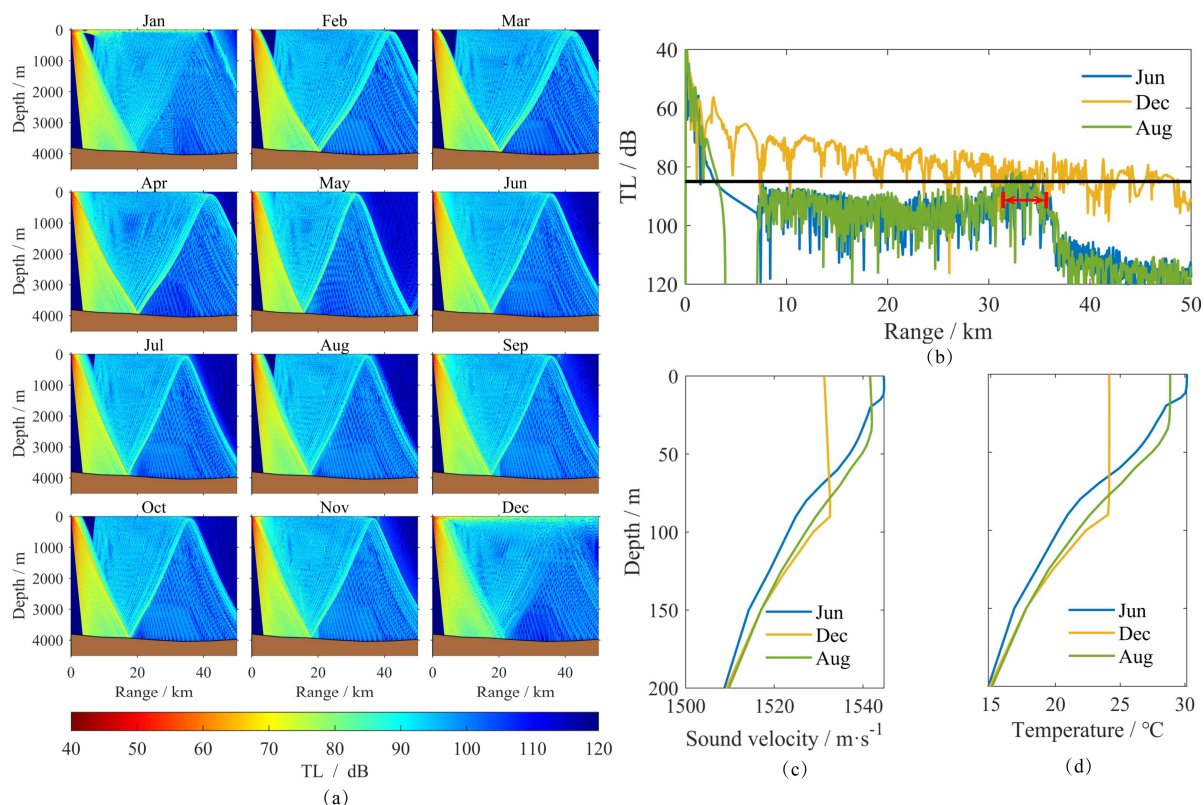


Figure 7. Analysis of sound propagation in the Deep-Sea Region (Point 70). (a) Two dimensional sound propagation loss; (b) Sound propagation loss curve; (c) Sound velocity profile; (d) Temperature profile.

4. Discussion

The Luzon Strait is commonly recognized as a region characterized by relatively frequent mesoscale oceanographic phenomena [12]. Consequently, underwater acoustic detection activities within this area are subject to the influence of intricate marine environmental dynamics [25,31]. The interpretation of such fluctuations to inform the practical deployment of sonar systems necessitates a specialized understanding of the marine acoustic environment. During maritime anti-submarine and other related detection operations, comprehensive real-time marine data are often not readily accessible, and there is a pronounced requirement for expediency in the evaluation of the DR. Thus, the present study endeavors to employ the Bellhop modeling approach to elucidate the general patterns of temporal and spatial variability in the DR within the maritime domain under consideration. This endeavor aims to facilitate the practical utilization of limited data to derive a reference value for the DR, which holds considerable practical significance. Consequently, based on the analyses previously presented, this study has identified the MLD and water depth as the two primary factors for the subsequent discussion on the variations in the DR.

Four distinct scenarios of MLD were chosen: 10 m, 30 m, 50 m, and 70 m. The observed data for the DR over a 5-year period (represented as scattered points in Figure 8) were then fitted against the variation of the water depth. The fitting outcomes are presented as curves within Figure 8. For the MLD values of 10 m and 30 m, the fits of the DR with respect to the depth are commendable, with relatively diminutive root mean square errors (RMSEs) of 1.5489 and 1.619, respectively. Initially, the DR escalates with the augmentation of the water depth; however, beyond a certain depth threshold (approximately 1000 m), the DR commences to diminish with the increase in the depth. As the depth extends to approximately 3000 m, the alteration in the DR stabilizes.

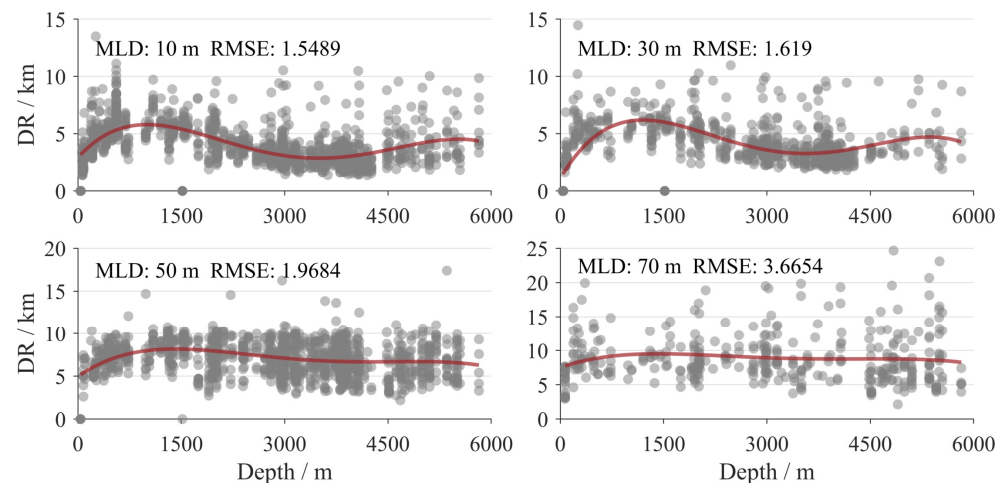


Figure 8. Statistics on the variation pattern of the DR with water depth.

For the MLD values of 50 m and 70 m (when the acoustic source is situated within the mixed layer), this modal of the DR variation is almost entirely eliminated, with the scattered points being exceedingly dispersed. The RMSE values are 1.9684 and 3.6654, respectively, suggesting that as the MLD converges upon and surpasses the depth of the acoustic source, water depth ceases to be a determinant in the fluctuation of the DR.

For the four experimental sites selected, the observed data concerning the DR were fitted against the variations in the MLD, as depicted in Figure 9. When the MLD ranges from 0 to 40 m, the acoustic source is not within the mixed layer and is distant from the bottom of the mixed layer. Consequently, the mixed layer exerts minimal influence on the sound paths, resulting in a negligible increase in the DR with the increase in the MLD. When the MLD ranges from 40 to 50 m, the bottom of the mixed layer approaches the depth of the acoustic source. In this interval, obliquely upward-directed acoustic rays with large grazing angles can be influenced to form surface ducts, leading to a rapid increase in the

DR. When the MLD exceeds 50 m, the acoustic source is completely within the mixed layer. Most of the sound rays emitted from the source can be influenced to form surface ducts for propagation, leading to an even faster increase in the DR. The RMSEs of the fitting results at the four experimental sites do not exceed 1.9.

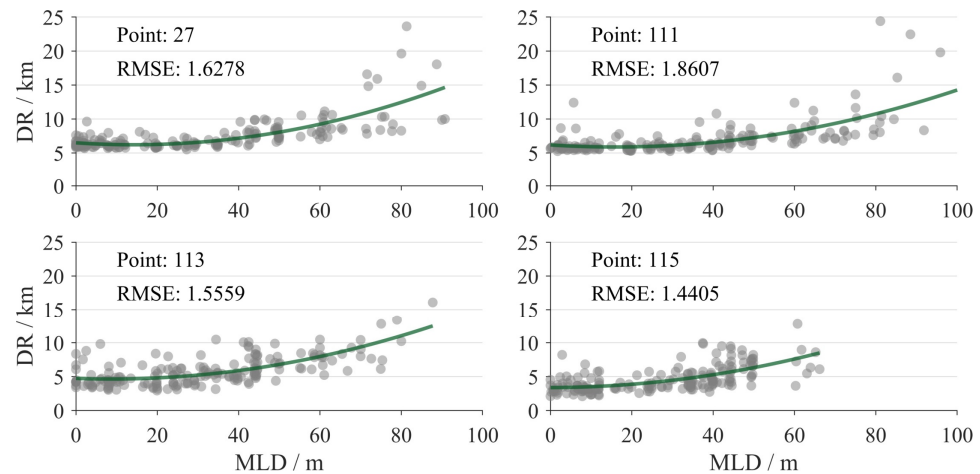


Figure 9. Statistics on the variation pattern of the DR with the MLD. (Point in the figure represents the position of experimental test point).

The fitting process utilized a comprehensive dataset of simulations spanning five years. At each experimental site, the fitting results exhibit a relatively small RMSE, suggesting that in the complex marine environment of the Luzon Strait, the utilization of the MLD and water depth as two primary factors can effectively elucidate the spatiotemporal variations in the DR. This understanding holds significant practical value, particularly in the context of submarine search route planning, where the rapid prediction of the DR based on limited information can enhance the search efficiency. For instance, a more universally applicable empirical formula can be established in this maritime area through the use of binary fitting methods. By employing the MLD and water depth to fit the empirical formula for the DR, following the separate fitting results presented earlier, the highest power of the independent variable MLD is set to 2 and the depth to 4. Utilizing the least squares method with all the calculated data, the fitting of the DR empirical formula yields the following result:

$$\begin{aligned}
 DR_f = & p_{00} + p_{10}MLD_R + p_{20}MLD_R^2 \\
 & + p_{11}MLD_R \cdot d_R + p_{12}MLD_R \cdot d_R^2 + p_{13}MLD_R \cdot d_R^3 \\
 & + p_{21}MLD_R^2 \cdot d_R + p_{22}MLD_R^2 \cdot d_R^2 \\
 & + p_{01}d_R + p_{02}d_R^2 + p_{03}d_R^3 + p_{04}d_R^4
 \end{aligned} \quad (13)$$

where MLD_R and d_R are the normalized values of the MLD and water depth, respectively, and the values of the parameters in the equation are listed in Table 1.

Table 1. Empirical formula parameters.

p_{ij}	$i = 0$	$i = 1$	$i = 2$
$j = 0$	4.325	1.421	0.5278
$j = 1$	−2.173	0.5881	0.007674
$j = 2$	1.852	−0.2314	0.00438
$j = 3$	1.095	−0.2371	
$j = 4$	0.7718		

Equation (12) was utilized to predict the DR (columns b and d) for each month of 2020, which was then compared against the simulated values (columns a and c) as depicted in Figure 10. Figure 11 illustrates the density scatterplot of the prediction results, with the scatter points clustering around the 1:1 line. The predicted values from the empirical

formula reflect the spatiotemporal changes in the DR within the study area. Moreover, this method has lower requirements for the input data compared to the sonar equation calculation method and has streamlined the process.

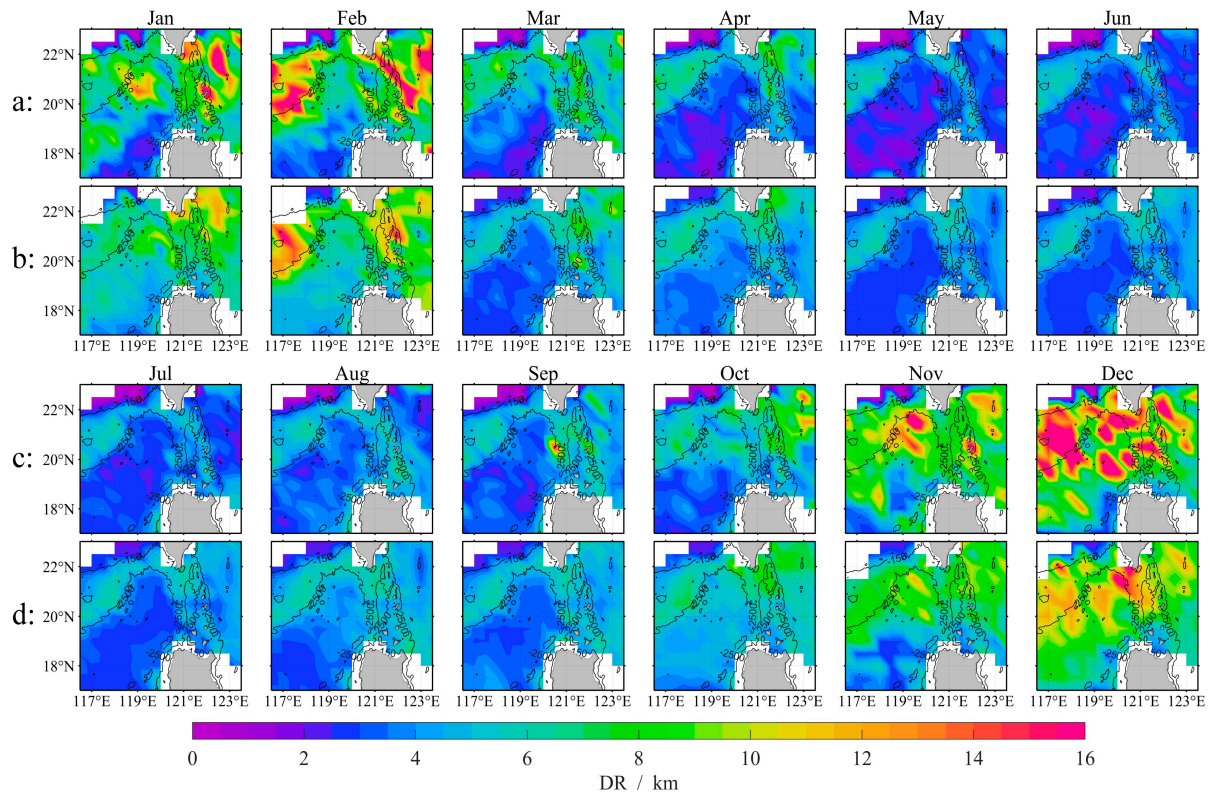


Figure 10. Comparison between empirical formula prediction results (columns (b,d)) and simulation results (columns (a,c)) in 2022.

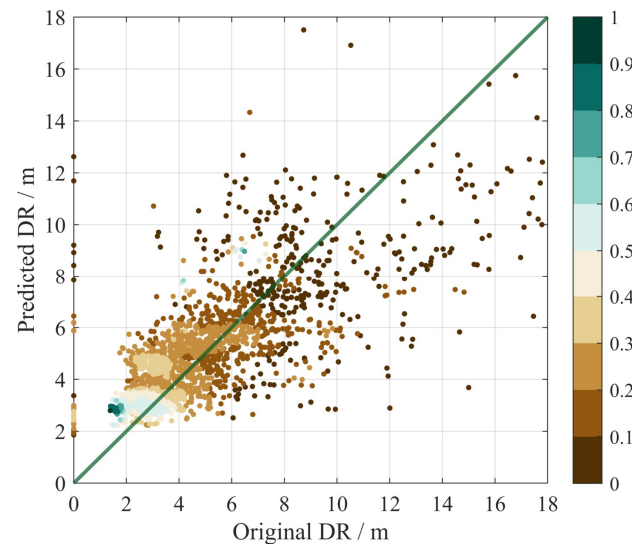


Figure 11. Density scatterplot. The solid green line in the figure is a 1:1 line, and the color represents the density of the scattered points.

This study provides a succinct description of the feasibility of predicting the DR using limited data. In reality, after identifying the primary influencing factors of the DR through statistical analysis, predictive models can be constructed using intelligent methods such as neural networks [32,33], enabling rapid prediction. This approach will offer significant practical assistance for maritime detection activities.

5. Conclusions

Analysis of the spatiotemporal distribution of the sonar detection range in the Luzon Strait yields the following conclusions:

1. During the summer and autumn seasons, when the mixed layer is shallow and a surface sound channel cannot form, the DR is primarily influenced by the water depth. In the Shallow Water Zone (<150 m), acoustic waves undergo frequent reflections between the sea surface and the seabed, resulting in significant energy loss and maintaining a low DR throughout the year. In the Intermediate Depth Zone (150–2500 m), the acoustic rays retain considerable energy after the first reflection from the seabed, enabling a DR of up to 5–8 km. As the water depth increases (>2500 m), the acoustic energy after the seabed reflection no longer satisfies the detection requirements, resulting in a DR of 2–5 km.
2. During winter and spring, the thick mixed layer is capable of forming a surface sound channel, which becomes the primary factor influencing the DR. In these seasons, the DRs are generally larger, with maximum values exceeding 10 km.

This study primarily analyzes the temporal and spatial variations of the sonar DR in the Luzon Strait. Furthermore, it briefly discusses the necessity and feasibility of rapidly predicting the DR using limited data. However, the patterns and conclusions drawn in this study are specific to the Luzon Strait. Future research should focus on the development of predictive models and their generalizability. Additionally, how to utilize the prediction results for search path planning to enhance the search efficiency remains an unresolved issue.

Author Contributions: Conceptualization, L.Z. and Y.W.; methodology, G.Z.; software, Y.M.; validation, X.Z.; formal analysis, G.Z. and Y.Y.; writing—original draft preparation, G.Z.; writing—review and editing, L.Z.; funding acquisition, L.Z. All authors have read and agreed to the published version of the manuscript.

Funding: This research received no external funding.

Data Availability Statement: The original temperature and salinity data presented in the study are openly available in HYCOM at https://tds.hycom.org/thredds/catalogs/GLBy0.08/expt_93.0.htm (accessed on 1 April 2024). The original temperature and salinity data presented in the study are openly available in ETOPO2022 at <https://www.ncei.noaa.gov/products/etopo-global-relief-model> (accessed on 1 April 2024).

Acknowledgments: This study acknowledges the provision of temperature and salinity data by HYCOM and bathymetric data by the U.S. National Geophysical Data Center. The contributions of these organizations have been instrumental in supporting the research objectives and analysis presented herein.

Conflicts of Interest: The authors declare no conflict of interest.

Dual-use Research Statement: We have made the following statements to our paper titled “Spatiotemporal Analysis of Sonar Detection Range in Luzon Strait”.

- Ø Explanation of Potential Risks: Our paper examines the sonar detection range in the Luzon Strait. This research is confined to comprehending the spatiotemporal variations of the acoustic propagation environment in the said maritime area and does not pose a threat to public health or national security.
- Ø Evaluation of Benefits to the General Public: Our research is limited to the academic field, which is beneficial to the development of oceanography. There is no risk to the general public.
- Ø Compliance with Laws: As an ethical responsibility, we strictly adhere to relevant national and international laws about dual-use research. And we have considered and adhered to these regulations in our paper.

References

1. Zhang, C.; Xiao, F. Overview of Data Acquisition Technology in Underwater Acoustic Detection. *Procedia Comput. Sci.* **2021**, *188*, 130–136. [\[CrossRef\]](#)
2. Shen, Z.; He, Y.; Liu, F. Position defining and Action of Towed Sonar Warship For Surface Force Formation. *Comput. Simul.* **2012**, *29*, 49–52.
3. Guo, Y.; Ai, R.; Chen, Y.; Qi, Y. Prediction of Passive Sonar Detection Range in Different Detection Probability. In Proceedings of the 2018 5th International Conference on Systems and Informatics (ICSAI), Nanjing, China, 10–12 November 2018; pp. 1289–1293.
4. Hodges, R.P. *Underwater Acoustics: Analysis, Design and Performance of Sonar*; John Wiley & Sons: Hoboken, NJ, USA, 2011.
5. Wu, Y.; Zhuo, X.; Tang, L.; Wu, W.; Qu, F. Cooperative Coverage Path Planning for AUVs in Integrated Underwater Acoustic Communication and Detection Networks. In Proceedings of the 2023 IEEE/CIC International Conference on Communications in China (ICCC), Dalian, China, 10–12 August 2023; pp. 1–6.
6. Li, B.; Chiong, R.; Gong, L. Search-evasion path planning for submarines using the Artificial Bee Colony algorithm. In Proceedings of the Evolutionary Computation, Beijing, China, 6–11 July 2014.
7. Panda, M.; Das, B.; Subudhi, B.; Pati, B.B. A Comprehensive Review of Path Planning Algorithms for Autonomous Underwater Vehicles. *Int. J. Autom. Comput.* **2020**, *17*, 321–352. [\[CrossRef\]](#)
8. Jiang, C.; Li, J.; Xu, W. Joint Detection and Tracking via Path Planning in the Mobile Underwater Sensing Network. In Proceedings of the 2018 10th International Conference on Wireless Communications and Signal Processing (WCSP), Hangzhou, China, 18–20 October 2018; pp. 1–6.
9. Germond, B. *The (Critical) Geopolitics of Seapower*; Palgrave Macmillan: London, UK, 2015.
10. Bilden; Philip, M.; Stavridis, J. Sea Power: The History and Geopolitics of the World's Oceans. *Nav. War Coll. Rev.* **2017**, *70*, 16.
11. Strategic rivalries around the Bab el-Mandeb Strait. *Dubai Med. J.* **2018**, *24*, viii–x.
12. Jiang, Y.; Zhang, S.; Tian, J.; Zhang, Z.; Gan, J.; Wu, C.-R. An Examination of Circulation Characteristics in the Luzon Strait and the South China Sea Using High-Resolution Regional Atmosphere–Ocean Coupled Models. *J. Geophys. Res. Ocean.* **2020**, *125*, e2020JC016253. [\[CrossRef\]](#)
13. Wang, J.; Yu, F.; Nan, F.; Ren, Q.; Chen, Z.; Zheng, T. Observed three dimensional distributions of enhanced turbulence near the Luzon Strait. *Sci. Rep.* **2021**, *11*, 14835. [\[CrossRef\]](#)
14. Liu, J.; Piao, S.; Gong, L.; Zhang, M.; Guo, Y.; Zhang, S. The effect of mesoscale eddy on the characteristic of sound propagation. *J. Mar. Sci. Eng.* **2021**, *9*, 787. [\[CrossRef\]](#)
15. Li, J.; Huang, X.; Shi, Y.; Yang, Y.; Zhao, W. Effects of internal solitary waves on three-dimensional sound propagation and DOA estimation in the South China Sea. *Appl. Acoust.* **2023**, *212*, 109612. [\[CrossRef\]](#)
16. Liang, M.; Meng, H.; Chen, Y.; Lu, K. Effect of underwater acoustics–environmental complexity on sonar detecting range. *Ship Sci. Technol.* **2013**, *35*, 45–48.
17. Emerson, C.; Lynch, J.F.; Abbot, P.; Lin, Y.-T.; Duda, T.F.; Gawarkiewicz, G.G.; Chen, C.-F. Acoustic propagation uncertainty and probabilistic prediction of sonar system performance in the southern East China Sea continental shelf and shelfbreak environments. *IEEE J. Ocean. Eng.* **2014**, *40*, 1003–1017. [\[CrossRef\]](#)
18. Na, Y.; Cho, C.; Son, S.; Hahn, J. A study on the variations of water temperature and sonar performance using the empirical orthogonal function scheme in the East Sea of Korea. *J. Acoust. Soc. Korea* **2024**, *43*, 1–8. [\[CrossRef\]](#)
19. Ferla, C.; Porter, M.B. Receiver depth selection for passive sonar systems. *IEEE J. Ocean. Eng.* **1991**, *16*, 267–278. [\[CrossRef\]](#)
20. Cummings, J.A. Operational multivariate ocean data assimilation. *Q. J. R. Meteorol. Soc.* **2005**, *131*, 3583–3604. [\[CrossRef\]](#)
21. Cummings, J.A.; Smedstad, O.M. Variational data assimilation for the global ocean. In *Data Assimilation for Atmospheric, Oceanic and Hydrologic Applications (Vol. II)*; Springer: Berlin/Heidelberg, Germany, 2013; pp. 303–343.
22. Chassignet, E.P.; Hurlburt, H.E.; Smedstad, O.M.; Halliwell, G.R.; Hogan, P.J.; Wallcraft, A.J.; Baraille, R.; Bleck, R. The HYCOM (HYbrid Coordinate Ocean Model) data assimilative system. *J. Mar. Syst.* **2007**, *65*, 60–83. [\[CrossRef\]](#)
23. Ainslie, M.A. The sonar equations: Definitions, dimensions and units of individual terms. *J. Acoust. Soc. Am.* **2009**, *123*, 3346. [\[CrossRef\]](#)
24. Anslie, M.; Leighton, T. Sonar equations for planetary exploration. *J. Acoust. Soc. Am.* **2016**, *140*, 1400–1419. [\[CrossRef\]](#) [\[PubMed\]](#)
25. Liu1, Y.; Zhang, X.; Fu, H.; Qian, Z. Response of sound propagation characteristics to Luzon cold eddy coupled with tide in the Northern South China Sea. *Front. Mar. Sci.* **2023**, *10*, 1278333. [\[CrossRef\]](#)
26. Li, L.; Jin, X.; Lu, C.; Wei, Z.; Li, J. Modelling and simulation on acoustic channel of underwater sensor networks. *Wirel. Commun. Mob. Comput.* **2021**, *2021*, 8263600. [\[CrossRef\]](#)
27. Xiong, C.; Wang, X.; Xia, Q. Bellhop Model's Application on Efficiency Analysis of Towed Line Array Sonar. *Digit. Ocean. Underw. Warf.* **2020**, *3*, 135–139.
28. Liang, Z.; Meng, C.X.; Xiao, H.T. Comparison of Sound Propagation Characteristic between Deep and Shallow Water. *Appl. Mech. Mater.* **2014**, *577*, 1198–1201. [\[CrossRef\]](#)
29. Lorbacher, K.; Dommenges, D.; Niiler, P.P.; Köhl, A. Ocean mixed layer depth: A subsurface proxy of ocean–atmosphere variability. *J. Geophys. Res.* **2006**, *111*, C07010. [\[CrossRef\]](#)
30. Duan, R.; Yang, K.; Ma, Y.; Hu, T. A study of the mixed layer of the South China Sea based on the multiple linear regression. *Acta Oceanol. Sin.* **2012**, *31*, 19–31. [\[CrossRef\]](#)

31. Liu, Y.; Chen, Y.; Chen, W.; Meng, Z. Inversion of Sound Speed Profile in the Luzon Strait by Combining Single Empirical Orthogonal Function and Generalized Regression Neural Network. *IEEE Geosci. Remote Sens. Lett.* **2024**, *21*, 1–5. [[CrossRef](#)]
32. Zhou, L.; Zhang, R. A self-attention-based neural network for three-dimensional multivariate modeling and its skillful ENSO predictions. *Sci. Adv.* **2023**, *9*, eadf2827. [[CrossRef](#)]
33. Zheng, X.; Peng, X.; Zhao, J.; Wang, X. Trajectory Prediction of Marine Moving Target Using Deep Neural Networks with Trajectory Data. *Appl. Sci.* **2022**, *12*, 11905. [[CrossRef](#)]

Disclaimer/Publisher’s Note: The statements, opinions and data contained in all publications are solely those of the individual author(s) and contributor(s) and not of MDPI and/or the editor(s). MDPI and/or the editor(s) disclaim responsibility for any injury to people or property resulting from any ideas, methods, instructions or products referred to in the content.